Quantifying Charge Carrier Localization in PBTTT using Thermoelectric and Spectroscopic Techniques

Shawn A. Gregory,[1] Amalie Atassi,[1] James F. Ponder Jr.,[2] Guillaume Freychet,[3] Gregory M. Su,[4,5] John R. Reynolds,[1,6] Mark D. Losego,[1] Shannon K. Yee[2*]

1 School of Materials Science and Engineering, Georgia Institute of Technology, Atlanta, GA, 30332, USA.

2 George W. Woodruff School of Mechanical Engineering, Georgia Institute of Technology, Atlanta, GA, 30332, USA

3 NSLS-II, Brookhaven National Laboratory, Upton, New York, 11973, United States

4 Advanced Light Source, Lawrence Berkeley National Laboratory, Berkeley, California, 94720, United States

5 Materials Sciences Division, Lawrence Berkeley National Laboratory, Berkeley, California, 94720, United States

6 School of Chemistry and Biochemistry, Georgia Institute of Technology, Atlanta, GA, 30332, USA.

* Corresponding author: shannon.yee@me.gatech.edu

Abstract: Chemically doped poly[2,5-bis(3-alkylthiophen-2-yl)thieno[3,2-b]thiophene] (PBTTT) shows promise for many organic electronic applications, but rationalizing its charge transport properties is challenging because conjugated polymers are inhomogeneous, with convoluted optical and solid-state transport properties. Herein, we use the semi-localized transport (SLoT) model to quantify how the charge transport properties of PBTTT change as a function of iron (III) chloride $FeCl_3$ doping level. We use the SLoT model to calculate fundamental transport parameters, including the carrier density needed for metal-like electrical conductivities and the position of the Fermi energy level with respect to the transport edge. We then contextualize these parameters with other polymer-dopant systems and previous PBTTT reports. Additionally, we use grazing incident wide-angle x-ray scattering (GIWAXS) and spectroscopic ellipsometry (SE) techniques to better characterize inhomogeneity in PBTTT. Our analyses indicate that PBTTT obtains high electrical conductivities due to its quickly rising reduced Fermi energy level, and this rise is afforded by its locally high carrier densities in highly ordered microdomains. Ultimately, this report sets a benchmark for comparing transport properties across polymer-dopant-processing systems.

Keywords: redox doping, charge transport, electrical conductivity, organic electronics, conjugated polymers

ToC Image:

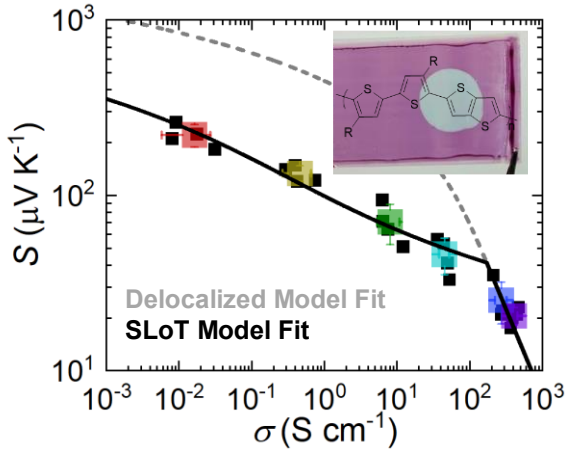

Introduction:

Semiconducting polymers are used in a variety of optical and electronic applications because of their synthetic tunability, mechanical compliancy, and processability.[1] One example is poly[2,5-bis(3-alkylthiophen-2-yl)thieno[3,2-b]thiophene] (PBTTT), which shows promise in many applications, such as thermoelectrics[2-4] and transistors.[5, 6] PBTTT is used in these applications because it is a solution processible conjugated polymer that has remarkably high carrier mobilities (μ ranging from ~ 0.1 to 10 $cm^2\ V^{-1}\ s^{-1}$, measured using multiple techniques)[7-10] and electrical conductivities (σ, ranging from 10^1 to $\gg 10^3$ $S\ cm^{-1}$),[10-19] depending on the doping and processing conditions (**Figure 1a**). Despite these high performing transport properties, it is not fully and quantifiably understood how and to what extent side-chain chemistry, dopants, and other processing conditions affect transport in PBTTT. Quantifying key parameters and characteristics that lead to these macroscopic transport properties is needed for the rational development of polymer-dopant-processing systems.

Charge transport models contextualize macroscopically measurable transport properties to microscopic spatial and energetic distributions and can provide insights into rational design. We have previously demonstrated that a semi-localized transport (SLoT) model can isolate and quantify localized (hopping-like) and delocalized (metal-like) contributions to the measurable electrical conductivity (σ) and Seebeck coefficient (S).[20] Central to charge transport models is the assertion of a transport function; for the SLoT model, the transport function, $\sigma_{\mathrm{E}}(E,T,c)$, is given as:

$$\sigma_{\mathrm{E}}(E,T,c) = \begin{Bmatrix} 0, & E_{\mathrm{t}} < 0 \\ \sigma_0 \exp\left(\frac{-W_H(c)}{k_B T}\right) \times \left(\frac{E-E_{\mathrm{t}}}{k_{\mathrm{B}} T}\right), & E_{\mathrm{t}} \geq 0, W_{\mathrm{H}} \geq 0 \\ \sigma_0 \times \left(\frac{E-E_{\mathrm{t}}}{k_{\mathrm{B}} T}\right), & E_{\mathrm{t}} \geq 0, W_{\mathrm{H}} < 0 \end{Bmatrix}. \quad (1)$$

This transport function quantifies the contributions of charge carriers at a specific electron energy level (E), temperature (T), and carrier ratio (c, the number of charge carriers per site, which is linearly related to the carrier density, n)[20, 21] to the measurable transport properties, σ and S.[22-24] Eq. 1 states that charge carriers at some energy level (E) less than the transport edge (E_{t}, which can be synonymous with a band edge and

the reference zero energy level, see illustrations in **Figure 1b**) do not contribute to the transport function nor to charge transport. In contrast, charge carriers that have some E greater than E_t contribute meaningfully to charge transport and their contribution is weighted by $\sigma_0 \exp\left(\frac{-W_H(c)}{k_B T}\right) \times \left(\frac{E-E_\mathrm{t}}{k_\mathrm{B} T}\right)$. σ_0 is independent of doping level, can ideally be related to the effective mass and energy independent mobility, and laterally shifts the $S(\sigma)$ curve.[22] The $\exp\left(\frac{-W_H(c)}{k_B T}\right)$ term captures the hopping-like contribution to charge transport due to the spatial and electrostatic localization of charge carriers in an inhomogeneous medium, such as a semiconducting polymer like PBTTT (see illustrations in **Figure 1b**).[25-28] For example, charge transport is likely greater along the conjugated backbones and between more ordered $\pi - \pi$ stacks, rather than between alkyl side chains and less ordered regions.[29-32] $W_H(c)$ is the localization energy, and it is calculable from macroscopic transport measurements; therefore, $W_H(c)$ represents a bulk ensemble average. $W_H(c)$ generally decreases as the carrier ratio, or carrier density, increases because the carriers' electrostatic potential wells increasingly impinge on one another and the barrier for hopping decreases (see illustrations in **Figure 1b**).[27, 29, 33, 34] Eventually, at some carrier ratio, W_H may be near negligible ($\lesssim k_\mathrm{B} T$ or zero), but all polymer-dopant-processing systems do not necessarily obtain these low W_H values.[34-36] If $W_\mathrm{H} \lesssim 0$, then localization is not the dominant physical contribution that explains $\sigma(T)$, the SLoT model asserts $\exp\left(\frac{-W_H(c)}{k_B T}\right) = 1$, and the transport function is dependent on only σ_0 and $\left(\frac{E-E_\mathrm{t}}{k_\mathrm{B} T}\right)$. Lastly, $\left(\frac{E-E_\mathrm{t}}{k_\mathrm{B} T}\right)$ captures the electron energy dependent contribution to the transport function, akin to delocalized and metal-like transport formalisms.[22-24] As the charge carrier ratio and density increases, the energy levels which charge carriers occupy (E) and the Fermi energy level (E_F) increase with respect to the transport edge (see illustrations in **Figure 1b**).

Evaluating the transport function with the Boltzmann transport equation yields expressions that relate the macroscopic and measurable σ and S values to these microscopic parameters and distributions detailed in Eq. 1.[22-24] The electrical conductivity expression is,

$$\sigma = \sigma_0 \exp\left(\frac{-W_H(c)}{k_B T}\right) \times \int_0^\infty \left(\frac{E-E_\mathrm{t}}{k_\mathrm{B} T}\right)\left(-\frac{df}{dE}\right) dE, \quad (2)$$

and Eq. 2 is a function of the energetic distribution of the charge carriers and their localization. As the extent of doping increases, localization decreases and the energy levels that charge carriers occupy increases, leading to large increases in σ. The Seebeck coefficient expression is,

$$S = \frac{k_B}{e}\frac{\int_0^\infty \left(\frac{E-E_t}{k_B T}\right)\left(\frac{E-E_t}{k_B T}-\eta\right)\left(-\frac{df}{dE}\right)dE}{\int_0^\infty \left(\frac{E-E_t}{k_B T}\right)\left(-\frac{df}{dE}\right)dE}, \quad (3)$$

where $\eta = \frac{E_F - E_t}{k_B T}$, is known as the reduced Fermi energy level, and represents the energetic distance between the Fermi energy level (E_F) and the transport edge (see illustrations in **Figure 1b**). Notably, Eq. 3 is only a function of the energetic distribution of the charge carriers and is not a function of σ_0 nor W_H. Therefore, there is only one η value and one set of Fermi integral values for Eq. 3 to be true at a fixed and measured Seebeck coefficient.[24] Furthermore, by measuring $\sigma(T)$ and $S(T)$ and by calculating the Fermi integral values, W_H and σ_0 in Eq. 2 are calculable at each doping level. Therefore, all SLoT model parameters are calculable from experimental measurements. With the SLoT model, one can isolate the interrelationships between macroscopic transport properties, fundamental transport parameters (*e.g.* $\sigma_0, \eta(c), W_H(c)$), and other physical observables (*e.g.* interchain distances, doping level, dopant intercalation).

Herein, we measure the charge transport properties of a n-dodecyl functionalized PBTTT doped with iron(III) chloride ($FeCl_3$) and use the SLoT model to benchmark its charge transport properties for the first time (**Figure 1 a,b**). Furthermore, we contextualize the PBTTT SLoT parameters by comparing with other polymer-dopant-processing systems. Lastly, we expand the SLoT model and its physical significance by performing grazing incidence wide angle x-ray scattering (GIWAXS) and spectroscopic ellipsometry (SE) measurements (**Figure 1c**). With these techniques, we find that the localization energy is independent of paracrystalline disorder and that the carrier density in metal-like microdomains are likely higher than that of the macroscopic average.

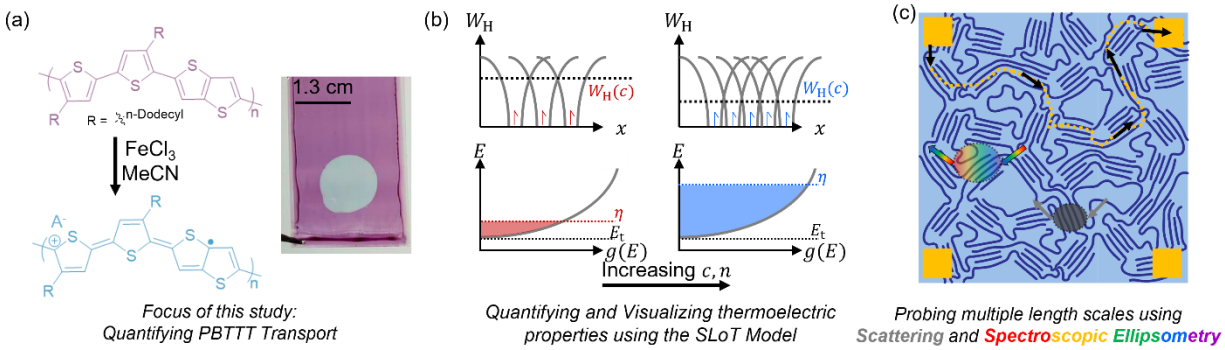

Figure 1: Visual summarizing the key facets of this study. (a) Neutral PBTTT-C12 (purple) is sequentially doped with $FeCl_3$ at various concentrations to control the extent of oxidation and resulting thermoelectric properties. Oxidatively doped PBTTT (blue) contains polaronic charge carriers (likely a combination of polarons and bipolarons) and distinctly different electronic and optical properties (see inset for a digital photograph of neutral PBTTT with a doped circular region). (b) The SLoT model is used to contextualize the thermoelectric properties of PBTTT at various doping levels. At low $FeCl_3$ concentrations and low extents of oxidation, PBTTT is lightly doped, the density of states, $g(E)$, is lightly filled with mobile charge carriers, has a low reduced Fermi energy level, η, and the charge carriers are spatially localized with high hopping activation energies, W_H (see leftmost figures in red). In contrast, at high $FeCl_3$ concentrations and high extents of oxidation, PBTTT is heavily doped, the density of states is heavily filled with mobile charge carriers, has a high reduced Fermi energy level, and the charge carriers can be thought as spatially delocalized with little-to-no hopping activation energies. (c) Cartoon illustrating different measurement techniques and their interaction area and conditions. Thermoelectric measurements, represented by gold square contact pads and dashed gold percolated transport pathway, are indicative of the appropriately weighted bulk ensemble average charge transport in all inhomogeneous microdomains along a closed circuit and percolated pathway. In contrast, scattering and spectroscopic measurements can glean insight on microstructure and transport properties in specific microscopic domains that do not require a closed circuit and percolated pathway but may require other physical conditions to be met (e.g., periodic ordering for Bragg diffraction).

Methods:

PBTTT-C12 was prepared via a Migita-Kosugi-Stille (Stille) polymerization, as outlined in **Note S1**. The repeat unit structure was confirmed with ^{1}H-NMR, as shown in **Figure S1**, and is consistent with previous reports.[37] The molecular weight and dispersity (M_n = 102 kg/mol, $Đ$ = 1.8, seen in **Figure S2**) of this polymer were estimated by gel permeation chromatography (GPC) in 1,2,4- trichlorobenzene (TCB) at 140 °C relative to narrow polystyrene standards. Electrochemical measurements show that the onset of electrochemical oxidation, and the redox estimated ionization potential value dictating it, is comparable to previous reports (**Figure S3**).[37]

PBTTT-C12 thin films (*ca.* 100 nm thick) were prepared by wire bar coating from chlorobenzene onto glass substrates and then thermally annealed at 180 °C for 20 minutes, unless otherwise stated. Films were sequentially doped by dropping a $FeCl_3$ -acetonitrile solution onto the film and allowing the film to oxidize. After oxidation, films were rinsed with excess acetonitrile to remove excess dopant and doping byproducts and then vacuum dried to remove solvent. **Figure 1a** shows the chemical structures and a representative digital photograph that shows pristine PBTTT with a subsection doped with and 50 mM $FeCl_3$. Cursorily, we note that doping alters the optical absorbance of the film, which will be detailed in subsequent sections. In general, sets of films were doped and then immediately measured to mitigate ambient environment and temporal effects. Additional procedural details and pristine PBTTT characterizations are in **Note S1**.

Results and Discussion

SLoT Modeling of PBTTT

Figure 2a shows σ and S for PBTTT-C12 as a function of the sequential doping $FeCl_3$ solution concentration. The $FeCl_3$ solution concentration was systematically swept from 0.5 to 50 mM to access a wide range of extents of oxidation and thermoelectric transport properties. At 0.5 mM $FeCl_3$ the PBTTT films show low σ (~ 0.01 S cm^{-1}) and high S (~ + 200 μV K^{-1}), indicating that these films are p-type and lightly doped. With increasing $FeCl_3$ concentration, σ increases and S decreases, which is consistent with the expected $S - \sigma$ anticorrelation and indicates higher carrier densities.[20] At 50 mM, PBTTT films show a high σ (420 ± 45 S cm^{-1}) and low S (20 ± 2.3 μV K^{-1}), consistent with several other PBTTT reports.[10, 13, 14, 17] We note that higher σ and lower S values have been reported in highly oriented thin films[11, 12, 18] that can be attributed to a more ordered microstructure (improved inter-chain transport) and to a broadened electronic structure with better orbital overlap.[38, 39]

To quantify the effects of $FeCl_3$ doping concentration on the electronic structure and extent of doping, ultraviolet-visible-near infrared (UV-Vis-NIR) and X-ray photoelectron spectroscopic (XPS) measurements were performed. **Figure 2b** shows the UV-Vis-NIR spectra for PBTTT films at each $FeCl_3$ solution concentration. As the $FeCl_3$ concentration increases, the pristine $\pi - \pi^*$ optical transition at 2.4 eV bleaches and polaronic absorbances at 1.5 eV emerges and increases, consistent with previous reports[13] and our measured thermoelectric trends. Additionally, in the range of 3 to 4 eV, two peaks emerge and increase in intensity with increasing doping level. These peaks are attributed to $FeCl_4^-$ counterions, which are Coulombically associated with positive polaronic charge carriers.[15] In **Figures S5, S6** we deconvolute these peaks and use known extinction coefficents[15, 40] to calculate the molar ratio of $FeCl_4^-$ counterions to BTTT repeat units and then the charge carrier volumetric density.[15] At 50 mM $FeCl_3$, we calculate a molar ratio of 0.80 ± 0.08 charge carriers per BTTT monomer. This molar ratio is equivalent to a charge carrier ratio of 0.4 (assuming two charge carriers per PBTTT monomer),[14] and a carrier density of 7.6×10^{20} carriers cm^{-3} (see **PBTTT-SLoT.xlsx** supporting information for calculations).[14] The value of 0.80 ± 0.08 charge carriers per BTTT monomer when doped with 50 mM $FeCl_3$ and measured using optical spectroscopies is consistent and within error of the XPS measurements and analysis (**Figure 2c,d, Figure S7**), and the presence of $FeCl_x$ counterions in the films are confirmed using survey and elemental spectra (**Figure S8, Table S1**). These XPS measurements show that oxidizing PBTTT with 50 mM $FeCl_3$ results in an increased signal at higher binding energies with respect to the pristine and neutral S-2$p_{3/2}$ signal. Using previously established deconvolution procedures,[20, 29, 35, 41-43] we calculate that this oxidized sulfur signal is approximately 24% of the total signal in the S-2p spectra (S/S_{ox} ~ 0.24, **Figure 2d**). Therefore, the XPS deconvolution indicates that approximately 1 out of every 4 sulfurs in PBTTT are oxidized, or a molar ratio of 0.96 charge carriers per BTTT monomer. Additionally, this maximum carrier density of 7.6×10^{20}

carriers cm^{-3} is approximately 2× greater than those in PBTTT-F4TCNQ studies,[7, 10, 40] and a PBTTT-TFSI OECT study,[14] and BTTT copolymer doped with F4TCNQ (ranged from $3\text{-}5 \times 10^{20}$),[21] but this carrier density is consistent with several PBTTT-$FeCl_3$ studies (ranging from 5.8×10^{20} carriers cm^{-3} to 9×10^{20} carriers cm^{-3}). [12, 15, 44] While some of the differences in the calculated carrier densities could be attributed to measurement methods and assumptions (e.g., UV-Vis-NIR, XPS, AC Hall), this spread in carrier densities is also likely a function of processing conditions (e.g., dopant chemistry and reduction potential) and the resulting microstructure (*vide infra*).

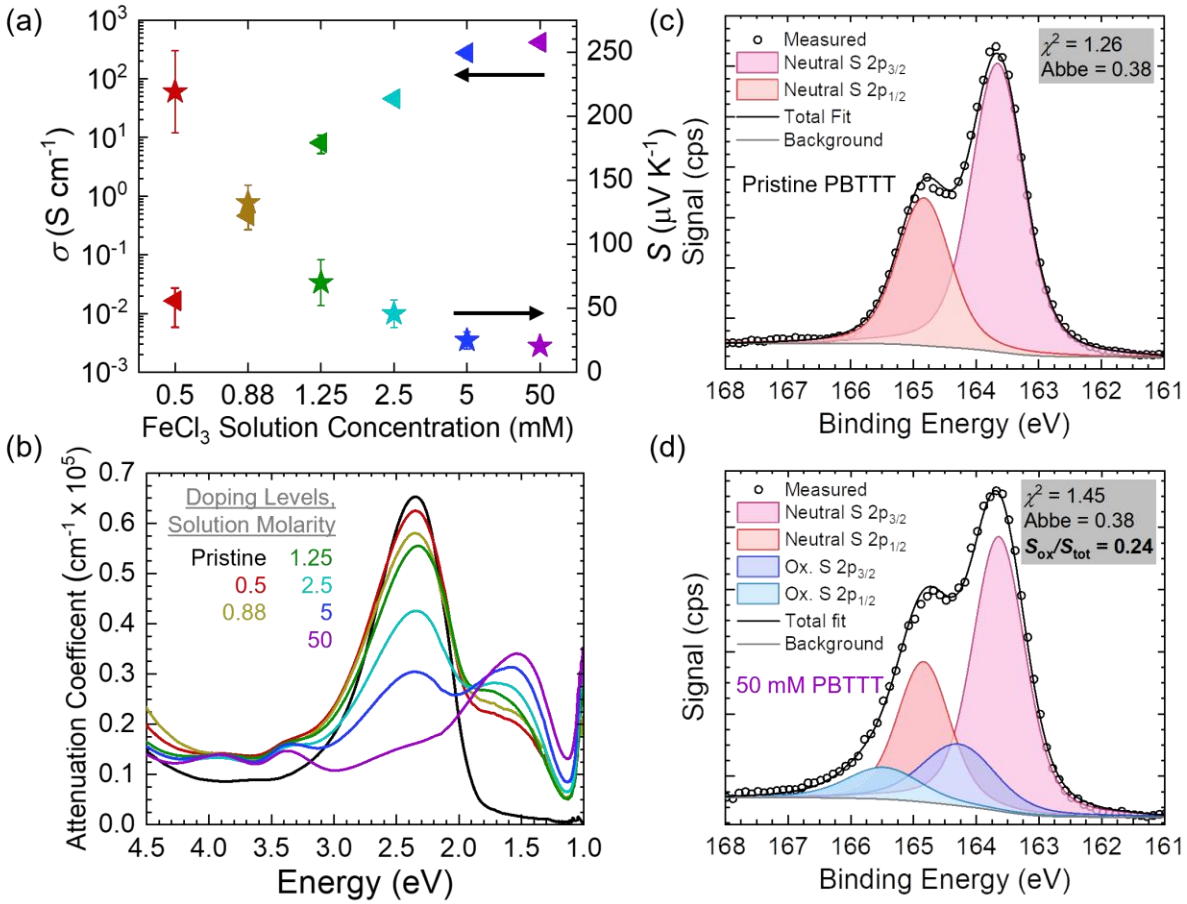

Figure 2: Quantifying nominal thermoelectric properties, optical properties, and extent of doping for PBTTT-C12 doped with $FeCl_3$. (a) Electrical conductivity and Seebeck coefficient as a function of $FeCl_3$ solution concentration. Error bars represent the sample-to-sample standard deviation. (b) UV-Vis-NIR attenuation coefficient as a function of photon energy. (c) Pristine PBTTT-C12 XPS measurement and deconvolution. (d) 50 mM $FeCl_3$ doped PBTTT-C12 XPS measurement and deconvolution. The low χ^2 values, Abbe criterion, and residual signal (see **Figure S6**) provide a high level of confidence in these deconvolutions.

With these carrier ratios and thermoelectric measurements, we apply the SLoT model to gain deeper insights. **Figure 3a** shows σ_{E_0} and η as a function of c, as calculated using the thermoelectric and spectroscopic measurements from **Figure 2** and Eq. 1-3. σ_{E_0} is the transport function prefactor and can be calculated by dividing the measurable electrical conductivity by the calculated electrical integral (see the look-up table in **PBTTT-SLoT.xlsx**). **Figure 3a** shows that as c increases, σ_{E_0} exponentially increases and then plateaus near 25 S cm^{-1}. **Figure 3a** also shows that as c increases, η increases, and this is interpreted as charge carriers occupying increasingly higher electronic states with respect to the transport edge. Note that when $\eta > 0$, $\eta \sim \int_0^\infty \left(\frac{E-E_t}{k_B T}\right)\left(-\frac{df}{dE}\right) dE$, so η alone linearly increases σ. Lastly, we note that η increasing to a maximum of 14 (equivalent of E_F shifting by ~0.36 eV with respect to E_t at 300 K) is consistent with the ~ 0.3 eV shift intensity-weighted binding energies from XPS (**Note S3, Figure S7**);[42, 43] this indicates that a linear-energy dependent transport function (Eq. 1) reasonably describes the electronic structure with these chemistries and processing conditions, and that the shifts in η may be used to contextualize the electronic structure.

To quantify the extent of localization, the electrical conductivity and Seebeck coefficient were measured as a function of temperature. At each temperature, σ_{E_0} was calculated from dividing the measured electrical conductivity by the Fermi integral value, and then W_H was calculated from the Arrhenius plot of $-\ln(\sigma_{E_0})\ vs. \frac{1}{k_B T}$ (**Figure 3b**). **Figure 3b** shows representative Arrhenius plots at low (0.88 mM), medium (2.5 mM) and high (50 mM) doping levels. **Figures 3b,c** show that the slope and calculated W_H values start high (greater than 100 meV), decrease to the order of 25 meV ($k_B T$ at 300 K), and continue to decrease to negative slopes (metal-like and thermally deactivated electrical conductivities).[20, 45] These metal-like W_H values calculated at high doping (5 and 50 mM) consistent with other reports on PBTTT.[17] Note that although W_H can be calculated to be less than zero from temperature dependent measurements, W_H is always modeled in Eq. 1 to be greater than or equal to zero because W_H captures the systematic decrease in σ due to localization effects.[20, 25] For each film and at each doping level, σ_0 is calculated from temperature dependent measurements, and **Figure S9** shows that σ_0 values are *ca.* 25 S cm^{-1}, on average, and do not have a statistically significant linear dependence on η. This is consistent with the plateauing of $\sigma_{E_0}(c)$.

Lastly, the $S(\sigma)$ anticorrelation is evaluated. **Figure 3d** plots the S, σ coordinates for each film and doping level averages. The solid black curve is calculated using the SLoT model (Eq. 1-3), using the experimental thermoelectric and carrier ratio measurements and their $\eta(c), W_H(c)$, and σ_0 regression parameters. This SLoT model curve has no freely adjustable values and accurately captures the experimental data. Additionally, the dashed grey curve represents the delocalized $S(\sigma)$ anticorrelation (*i.e.*

Kang-Snyder $s = 1$) which assumes that $\sigma_{E_0} = \sigma_0$ at all doping levels and that σ_{E_0} (and ergo W_H) does not change as a function of doping level.[23] Notably, the SLoT model and delocalized models become colinear when $W_H \lesssim k_B T$, and captures the data points that have little to no thermal activation at high doping levels. We note that the SLoT fit is calculated with no freely adjustable parameters in **Figure 3d**, and this fit is remarkably consistent with the SLoT fits previously predicted using previous literature data sets and an adjustable $W_H(c)$ relationship (**Figure S10**).[14, 17, 20] This consistency further affirms the use of the SLoT model to predict transport parameters from $S(\sigma)$ data when temperature and/or carrier dependent data is not available.

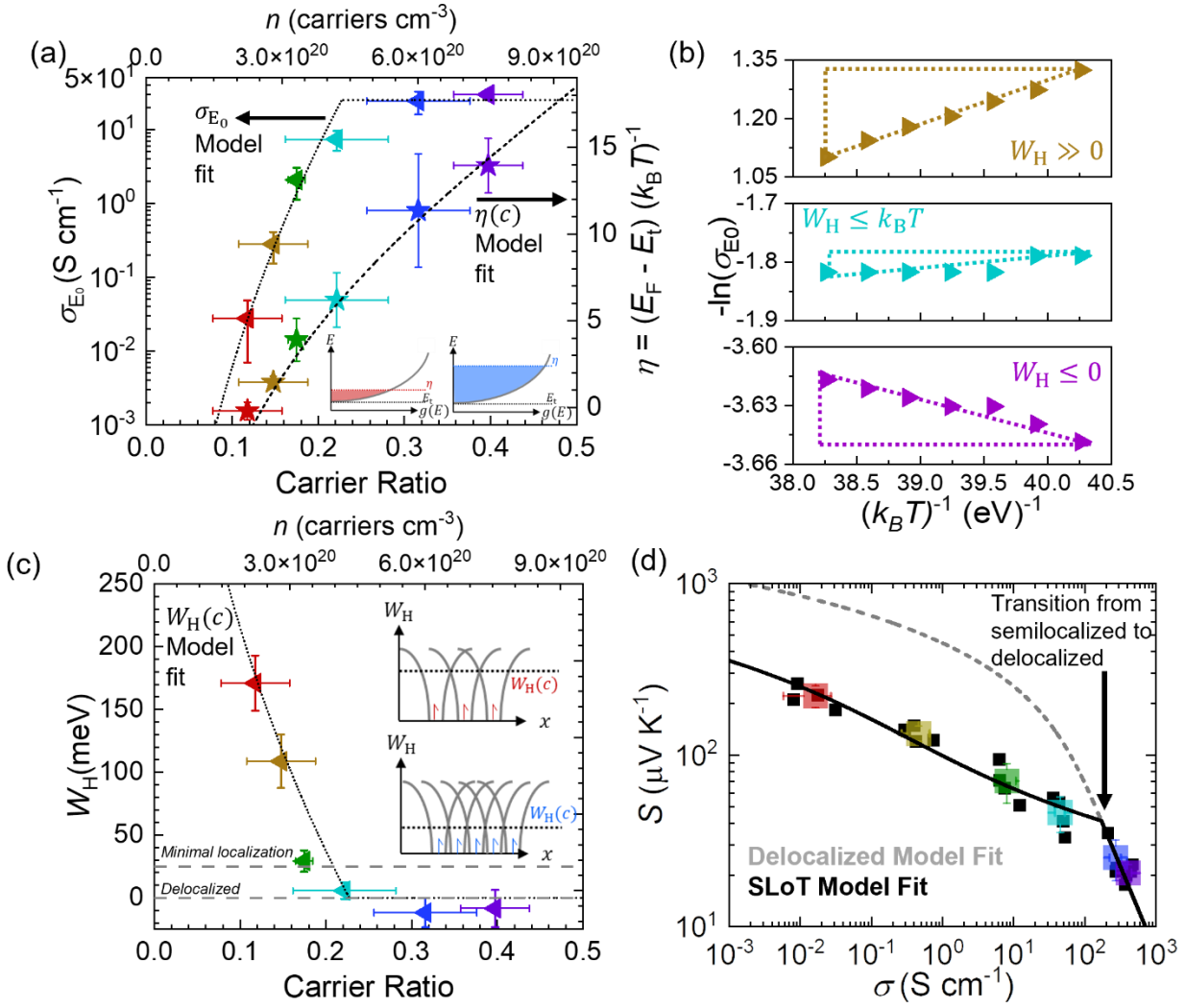

Figure 3: SLoT modeling of PBTTT-C12 sequentially doped with $FeCl_3$. (a) SLoT model transport function prefactor and reduced Fermi energy as a function of carrier ratio and density. Inset illustrates the interpretation of increasing η values, akin to Figure 1. (b) Representative Arrhenius plots, where the slopes are equal to W_H. Note that in this narrow temperature range (288 K – 303 K), the electrical conductivity (and ergo σ_{E_0}) oftentimes has a statistically significant temperature dependence while the Seebeck coefficient does not (ergo η does not observably vary). (c) Localization energy as a function of carrier ratio. Inset illustrates that localization decreases as carriers begin to spatially impinge, akin to Figure 1. Note that the carrier densities reported herein assume the carriers have a $+1e$ and do not transport as a pair (i.e., bipolaron); if all charges were bipolaronic in nature, then the n values in (a,c) would be halved of what is presently shown. (d) $S(\sigma)$ curve showing doping level average properties (colored squares, error bars represent sample to sample standard deviation), individual films properties (black squares), delocalized transport model (grey dashed line) and the SLoT model fit with no freely adjustable variables (black line). See Note S3 and PBTTT-SLoT.xlsx for additional details.

Developing microstructural-charge transport relationships

The SLoT model becomes more useful when coupled with additional characterization techniques. At minimum, the SLoT model requires temperature dependent thermoelectric and carrier density measurements, but these measurements do not quantify how the atomic structure and/or microstructure affect the resulting observables. Therefore, we now examine how GIWAXS furthers the utility of the SLoT model for this PBTTT-$FeCl_3$ system.

Figure 4a-d show representative two-dimensional diffractograms for pristine, 0.88 mM, 2.5 mM, and 50 mM doped films. These diffractograms show a high extent of ordering for a conjugated polymer system, with lamellar (h00) peaks up to a (400) reflection, consistent with previous reports on PBTTT.[8, 15] Furthermore, these diffractograms show that the crystallite lamellar stacking direction is predominantly along the out-of-plane direction (q_z axis), the (003) intra-chain spacing is predominantly along the nearly-in-plane (q_{xy}) axis. Additionally, there is a distribution of (110) interchain $\pi-\pi$ stacks, with a bimodal predominance near the two poles at all doping conditions. These orientations indicate that these PBTTT films are preferentially ordered edge-on with respect to the substrate; however, we note this extent of edge-on is qualitatively weaker than that reported in other studies, and may be because these films are thicker (hundreds of nanometers) compared to those commonly used in other studies (tens to hundred of nanometer).[15]

To gain deeper insight on these diffractograms, we analyzed radially integrated profiles (**Figure 4e**). These profiles show that as the extent of doping increases, the lamellar peaks shifts to small q values, indicating an expansion in real space from 18.7 Å to 20.6 Å, as shown in **Figure 4f**. Concomitantly, the $\pi-\pi$ stacks contract in real space from 3.58 to 3.45 Å, which suggests dopant intercalation in the side chain region, consistent with previous reports.[10, 15] The PBTTT-C12 reported here has smaller lamellar spacings compared to PBTTT-C14 (20 Å pristine, 26 Å $FeCl_3$ doped),[15] as expected, but has notably tighter $\pi-\pi$ stacks compared to previous PBTTT-C_x reports (~3.7 Å pristine, ~3.55 Å doped).[15, 17] These tighter $\pi-\pi$ stacks may be afforded by the smaller side chains and likely improves charge transport within crystalline domains. Furthermore, the quality of the crystalline domain can be evaluated using the

paracrystallinity (g) and the coherence length (L_c).[46-48] Detailed notes on the interpretation and calculations of g and L_c are found in the supporting information (**Note S4, Figures S11-12, Table S2**), and here we highlight two key findings. First, **Figure 4g** shows that g = 5.5%, on average, for this PBTTT-C12/$FeCl_3$ system in the (110) direction. This is a remarkably low level of paracrystalline disorder for a conjugated polymer (generally ~7–20%).[49] Therefore, we believe that the ordered domains are exceptionally well ordered and tightly packed, but this amount of order does not provide insight on percolation pathways between spatially separated domains. Second, we note that the amount of paracrystallinity (*i.e.* structural disorder) in the (110) direction varies slightly (~ 10%) as a function of doping level; but, the coherence length (*i.e.* crystallite size) in the (100) direction significantly decreases (-44%) with increasing doping level (**Figure 4g**). This indicates that $FeCl_3$ doping substantially decreases the quality of the ordering of the electrically insulating alkyl region, but doping does not as substantially affect the quality of the ordering of the electrically conductive $\pi - \pi$ stacking direction.

The fact that g is independent of doping level is quite notable because previous reports have linked (110) paracrystallinity to the broadening of the density of electronic states and the creation of trap and/or localized electronic states; these trap states have energetic breadths and field-effect thermal activation energies on the order of *ca.* 100 meV in the pristine polymer.[28, 46-50] Similarly, in the dilute carrier limit ($c \sim 0.1$), the localization energy (W_H) is within a factor of 2× as predicted using paracrystallinity models. Although g remains effectively constant with respect to doping level, we observe that W_H decreases significantly with increasing doping level. We hypothesize that this apparent discrepancy between g and W_H at higher doping levels is because the reduced Fermi energy levels (and transport properties) probed are not at the same energy levels where there is energetic disorder due to paracrystallinity. This hypothesis is reinforced by the fact that when PBTTT is "doped" using a field effect method (i.e. controlling the applied biases), PBTTT oftentimes obtains Seebeck coefficients on the order 700-1000 μV K^{-1},[51] which is akin to an η of -7 (~0.2 eV below E_t and ~0.55 eV below 50 mM $FeCl_3$ doped PBTTT herein). Therefore, this study suggests that the (110) paracrystallinity and structural disorder is not a significant contributing factor

to W_H at these degenerate doping levels, and we hypothesize the physical mechanisms that limit W_H in chemically doped semiconducting polymers are likely the electrostatic attraction of polaronic charge carriers to counteranions, polarization of the local bond order, and the spatial percolation of charge carriers on larger length scales (> ~10 nm).[20, 25, 27]

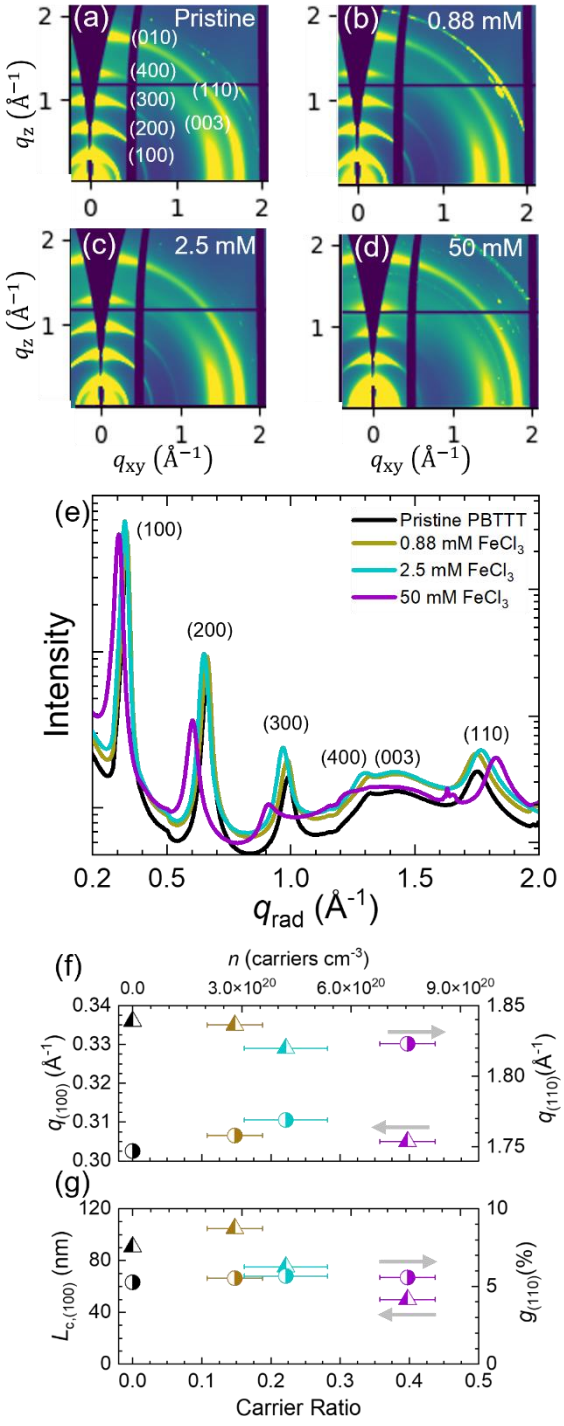

Figure 4: PBTTT-$FeCl_3$ GIWAXS measurements and analysis. Representative diffractograms for (a) Pristine, (b) 0.88 mM $FeCl_3$ doped, (c) 2.5 mM $FeCl_3$ doped, and (d) 50 mM doped PBTTT films. Pristine diffractogram shows annotated indices. (e) Radially integrated linecuts. (f) Lamellar (100) and $\pi - \pi$ q values. (g) Coherence length and paracrystallinity. Note that in (f) and (g), the top and bottom x-axes are the same for both plots and that the arrows correspond to the y-axis for each data series. Explicitly, the triangle data points correspond to the left y-axes while the circles correspond to the right y-axes.

Quantifying localization and charge transport using spectroscopic ellipsometry

The SLoT model uses macroscopic thermoelectric measurements to define transport parameters that represent an appropriately weighted average of the microscopic ensemble. Though SLoT allows us to model the macroscopic average, conjugated polymers are known to be inhomogeneous. Explicitly, the macroscopic σ is a single value, but it is known that there are regions within the polymer that have larger σ values that are likely electrically insulated (to some extent) by regions with smaller σ values.[30, 52, 53] This inhomogeneity has been used to improve charge transport and thermoelectric performance; for example, Ma *et al*. recently demonstrated that higher thermoelectric power factors are obtained by preferentially doping the ordered regions.[53] Although W_{H} is a useful tool to capture the macroscopic effects of localization, and GIWAXS is a useful tool to quantify the quality and spacing or molecular packing within crystalline domains, these approaches do not provide information on how the ordered domains are distributed and/or percolated throughout the film and their microscopic transport properties. Measurement techniques, such as atomic force microscopy,[52] scanning kelvin probe microscopy,[54] atom probe tomography,[55] and transmission electron microscopy,[56] can have sufficient spatial resolution to quantify inhomogeneous spatial distributions, but these techniques do not necessarily provide information on the microscopic transport properties. In contrast, there are reports that use thermal[57, 58] and dielectric properties[59-62] to contextualize the effects of percolation and effective medium inhomogeneity on the resulting $\sigma(n,T)$ and $S(n,T)$ properties.[63] Ultimately, we posit that spectroscopic ellipsometry measurements are useful for characterizing inhomogeneous materials with microscopic regions of varying transport properties.

Here, we explore the use of spectroscopic ellipsometry (SE) to quantify the complex dielectric function in PBTTT, model the dielectric-like and metal-like contributions to the observable optical properties, and relate these contributions to the measurable thermoelectric properties and SLoT parameters. The complex dielectric function is expressed as,

$$\epsilon(\omega) = \epsilon_1(\omega) + i\,\epsilon_2(\omega), \tag{4}$$

where $\epsilon_1(\omega)$ is the real component, and $\epsilon_2(\omega)$ is the imaginary component.[64] The complex dielectric function can link measurable optical properties, such as reflectivity, to the calculable material parameters, such as carrier densities. Additionally, $\epsilon_1(\omega)$ and $\epsilon_2(\omega)$ capture various physical processes such as charge polarization, interband optical transitions, and Drude-like charge transport.[64, 65]

SE measures the change in the ratio of the polarized light intensities ($\tan(\psi)$) and phases (Δ) upon reflection,[64, 66, 67] and these changes in ψ and Δ are related to $\epsilon_1(\omega)$ and $\epsilon_2(\omega)$ through an optical model. **Figure 5a** shows representative ψ and Δ values for pristine PBTTT and 50 mM $FeCl_3$ doped PBTTT with comparable thicknesses, and **Figure S13** shows ψ and Δ at each doping level. Clearly, the measurable ψ and Δ change due to doping, consistent with the prior characterizations, and this suggests that $\epsilon_1(\omega)$ and $\epsilon_2(\omega)$ also change. To quantify $\epsilon_1(\omega)$ and $\epsilon_2(\omega)$ in the PBTTT film, an empirical optical model was developed to fit the changes in ψ and Δ and extract the film's dielectric function (**Note S5** details the optical model). **Figure 5a** shows the B-Spline fits from the optical model agree well with the measured values, indicating that the $\epsilon_1(\omega)$ and $\epsilon_2(\omega)$ values calculated with the optical model for the PBTTT films are consistent with the experimental measurements.

Figure 5b-c plots the calculated $\epsilon_1(\omega)$ and $\epsilon_2(\omega)$ as a function of doping level and photon energy. ϵ_1 is associated with the ideal polarization of the film without losses, and ϵ_2 is associated with lossy processes such as heat generation, interband absorption, and free charge carrier absorption.[64, 65] The values for $\epsilon_1(\omega)$ and $\epsilon_2(\omega)$ (and their corresponding complex index of refraction values, $\tilde{n}$ and $\tilde{k}$, **Figure S14**) are reasonable and consistent with previous measurements on doped and pristine conjugated polymer films.[66-68] These consistencies give us a high level of confidence in the $\epsilon_1(\omega)$ and $\epsilon_2(\omega)$ calculations.

Most notable is that ϵ_1 in the 50 mM PBTTT shows regimes where $\epsilon_1 \lessapprox 0$ (**Figure 5b**). Typically, metals have negative ϵ_1 values due to free carrier attenuation at frequencies less than the plasma frequency and a positive ϵ_1 at frequencies greater than the plasma frequency due to polarization.[64] In contrast, Lorentz-like oscillators (*e.g.* band gap transitions) typically exhibit $\epsilon_1 > 0$. Because 50 mM doped PBTTT exhibits both positive and negative ϵ_1 values, it is likely that a combination of free-electron and optical transitions

are present, consistent with the UV-Vis-NIR measurements and thermoelectric measurements. This is qualitatively represented by the cartoon illustration in **Figure 1c,** where the spectroscopic ellipsometry is probing and measuring transitions in multiple spatial regimes. Furthermore, previous reports have also observed similar ϵ_1 behavior with PEDOT:PSS and PEDOT:Tos as a function of processing conditions and doping level (where ϵ_1 changes sign multiple times),[69-72] but these studies did not systematically vary the doping level from the pristine state to a fully doped state. Lastly, the optical transitions and ϵ_2 values in **Figure 5** are in good agreement between and the transmission attenuation in **Figure 2**. Both analyses show that absorption shifts to the infrared region and the visible region is increasingly bleached with increasing doping level.

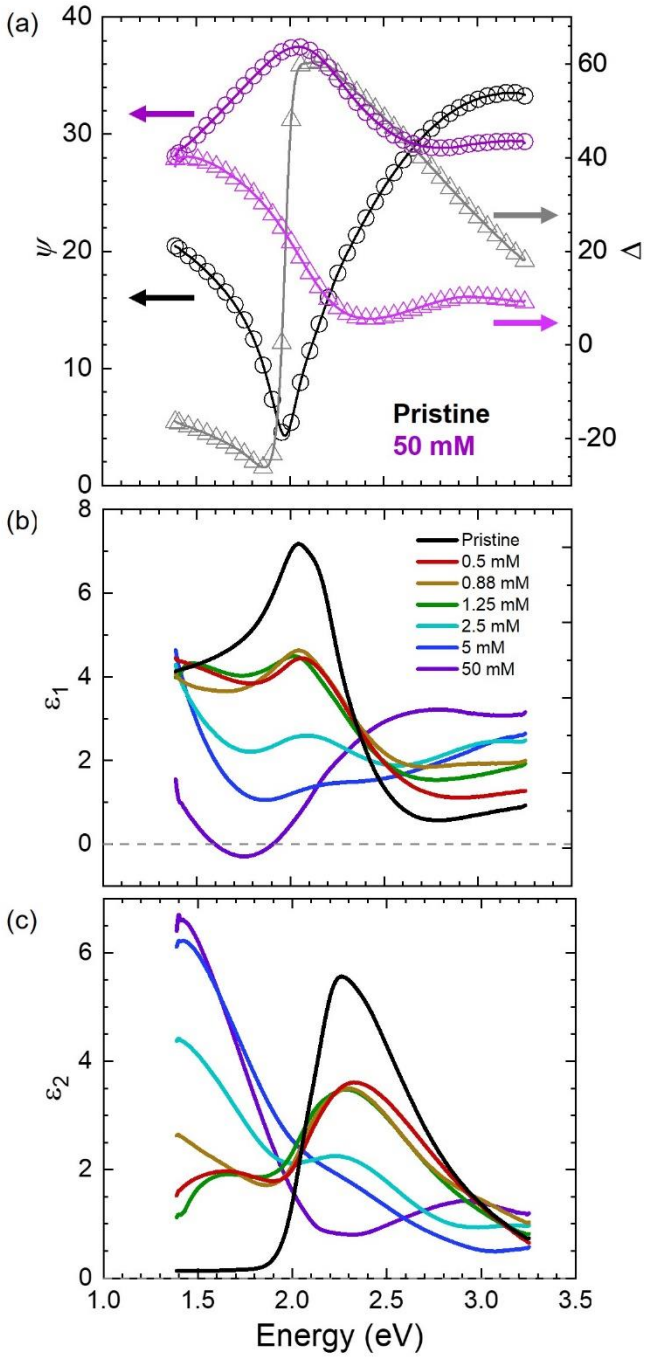

Figure 5: PBTTT-$FeCl_3$ spectroscopic ellipsometry measurements, B-spline fits, and complex dielectric function calculations. (a) Representative ψ and Δ measurements for pristine and 50 mM $FeCl_3$ doped PBTTT films with comparable thickness (~ 180 nm) on glass substrates. One out of every five measured data points are shown for clarity, and line represent the B-spline fitting, calculated using known substrate properties, known film thickness, and assumed Kramers-Kronig consistency. (b) Real component (ϵ_1) of the complex dielectric function. (c) Imaginary component (ϵ_2) of the complex dielectric function.

We now turn to deconvoluting $\epsilon(\omega)$ to better quantify the physical phenomena responsible for the optical transitions. By deconvoluting $\epsilon(\omega)$, we obtain fundamental transport properties such as the carrier density. Here, we deconvolute $\epsilon(\omega)$ using the simplest peak deconvolution models that account for polaronic transitions, free charge carriers, and $\pi - \pi^*$ transitions; however, we note that more complicated models exist that account for specific microgeometries (*e.g.*, core-shell, slabs, *etc.*), in- and out-of-plane contributions (*i.e.*, ordinary, and extraordinary), and grating.[65, 73, 74]

Overall, $\epsilon(\omega)$ has the functional form of,

$$\epsilon(\omega) \approx \epsilon_\infty - \left[\frac{\sigma}{\epsilon_0\left(\frac{\omega^2 m^* \mu}{e} + i\omega\right)}\right] - \left[\sum \frac{A_l}{(\omega^2 - \omega_l^2) + i\omega\gamma_l}\right]. \quad (2)$$

ϵ_∞ is the dielectric constant at approaching infinitely high frequencies, ϵ_0 is the permittivity of free space, ω is the angular frequency, A_l is the *l*-th Lorentzian absorption amplitude, ω_l is the resonant frequency of the *l*-th absorber, and γ_l is the absorption broadening. The first bracketed term accounts for Drude-like free carrier contribution, and the second bracketed term accounts for sum of *l*-number of oscillator transitions, such as $\pi - \pi^*$ optical, polaronic, and vibrational transitions.[73, 74] The second bracketed term is written in the form of a Lorentzian oscillator, but depending on the exact mechanism, the broadening of the Lorentz line shape may be more appropriately modeled using a single Gaussian, multiple Gaussians, Tauc-Lorentz, or Voigt distributions, to name a few.[74] By deconvoluting ϵ_1 and ϵ_2 at each doping level, the contribution of each oscillator and free-electron contribution can be systematically quantified.

Figure 6 shows a representative set of spectroscopic ellipsometry deconvolutions, which isolate the physical contributions to the dielectric loss function. **Figure 6a** shows the deconvolution for pristine PBTTT. The B-spline fit is well modeled using a single Cody-Lorentz peak, which captures the optical band gap, the $\pi - \pi^*$ transition. While Lorentzian peaks are symmetrical about the harmonic frequency, Cody-Lorentzian peaks are asymmetric about the harmonic frequency and account for more transitions above the harmonic frequency and a steeper cut-off for transitions below the harmonic frequency.[75] Although multiple peaks could be used to deconvolute the $\pi - \pi^*$ transition,[76] this becomes increasingly

cumbersome when deconvoluting the doped films as there are more free variables. Using the peak deconvolution settings from the pristine PBTTT, we then turn to quantifying the polaronic oscillator contribution. **Figure 6b** shows the deconvolution for 1.25 mM $FeCl_3$ doped PBTTT. At 1.25 mM, $\sigma, n,$ and μ values are likely too low to significantly contribute to the dielectric function in the UV-Vis-NIR region, but there is a polaronic peak near 1.5 eV, akin to **Figure 2**. This peak is well modeled using a simple Gaussian peak, like previous reports.[76] Lastly, **Figure 6c** shows 50 mM $FeCl_3$ doped PBTTT. Using the incremental change in the dielectric function at each doping level (**Figure 6**), we can begin to isolate the free electron contribution to ϵ_2. Notably, **Figure S15** shows that the 50 mM dielectric function cannot be as well modeled using a polaronic and $\pi - \pi^*$ oscillators alone; therefore, we conclude that the Drude free electron contribution is likely necessary. Additionally, this Drude-like contribution is needed to explain the slopes and curvatures in the mid-infrared (MIR) as shown in **Figure S6**. We note that the Drude contribution in the MIR is convoluted with polaronic absorbances (likely a combination of polaron and bipolaron contributions), and therefore this Drude contribution may be responsible for asymmetric peaks that decreases with increasing energy. Future spectroscopic ellipsometry measurements deeper in the mid-infrared and on additional highly electrically conductive polymers will increase the certainty of the Drude contribution in spatially inhomogeneous polymers.

This Drude contribution at 50 mM is modeled by using $n = 6 \text{ x } 10^{21}$ carriers cm^{-3} and $\sigma = 2{,}200$ S cm^{-1} (**Figure 6c**). Although this Drude contribution is consistent with spectroscopic ellipsometry data, it is seemingly inconsistent with the thermoelectric transport data which shows $n = 7.6 \text{ x } 10^{20}$ carriers cm^{-3} and $\sigma = 420$ S cm^{-1} (**Figures 2,3**). Interestingly however, we note that this ellipsometry carrier density is comparable to the carrier density recently reported using an AC Hall technique.[44] We believe that these substantial differences in transport properties is likely because the ellipsometry measurements are probing optical oscillators which are on smaller length scales compared to the macroscopic thermoelectric transport (**Figure 1c**). It is likely that the carrier densities and electrical conductivities calculated using the Drude component from ellipsometry deconvolutions are a more accurate representation for the electrically

conductive domains (likely crystalline regions of the $\pi - \pi$ stacks) whereas the carrier densities and electrical conductivities in **Figure 2,3** are better thought as bulk averages, which are systematically lowered by less ordered domains and insulating side chains. We note that PBTTT is ~50% insulating side chain by molecular weight, and we recently demonstrated that removing the side chains in dioxythiophene copolymers increases the measure σ by ~10× and n by ~2×.[29, 77] Furthermore, the Drude electrical conductivity modeled using ellipsometry is consistent with several reports that show σ in PBTTT is $>10^3$ S cm^{-1} when highly ordered.[12, 18, 19] This ellipsometry analysis suggests that highly electrically conductive PBTTT on the macroscale is afforded by a percolated series of highly ordered and Drude-like domains, and less electrically conductive PBTTT on the macroscale is due to highly ordered Drude-like domains being electrically isolated from one another. This percolation picture is akin with previous ellipsometry-charge transport reports that compared the differences in ϵ and σ as a function of evaporated Au film thickness,[61] atomic layer deposited Pt/Ru/Pd film thickness,[62] and the percolation of Ag nanoparticles in a strained elastomer.[60] Ultimately, this analysis shows that spectroscopic ellipsometry could be useful for complimenting structural and thermoelectric measurements and provides a more holistic picture for charge transport.

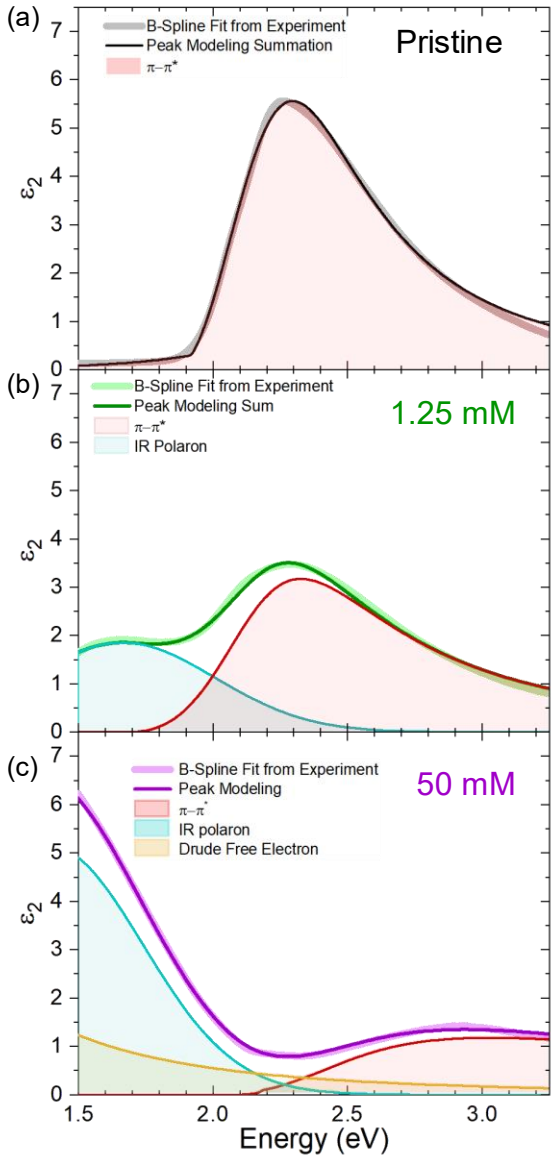

Figure 6: Representative spectroscopic ellipsometry deconvolutions as a function for PBTTT-$FeCl_3$ doping level. (a) Pristine PBTTT, modeled using only a Cody-Lorenz oscillator for the $\pi - \pi^*$ band gap transition. (b) PBTTT doped with 1.25 mM $FeCl_3$, modeled using a compared $\pi - \pi^*$ band gap transition and a Gaussian polaronic absorption. (c) PBTTT doped with 50 mM $FeCl_3$, modeled using a comparable $-\pi^*$ optical transition and polaronic absorption as well as a Drude free electron contribution. Additional deconvolution notes and methodologies are found in Note S5.

Conclusion:

The charge transport properties of chemically doped semiconducting polymers are difficult to holistically understand because spatial inhomogeneity leads to charge transport properties that vary significantly as functions of doping level and spatial coordinate. In this PBTTT-$FeCl_3$ study, we used the SLoT model to quantify fundamental transport parameters, such as σ_0, $W_{\mathrm{H}}(c)$, and $\eta(c)$, which can be used to robustly compare and design polymer-dopant-processing systems. Using GIWAXS measurements, we conjecture that PBTTT's highly conductive transport parameters are likely because of the smaller $\pi - \pi$ stacking distances that decrease with increasing doping level and have low levels of paracrystalline disorder. Using spectroscopic ellipsometry measurements and deconvolution, we quantify how the complex dielectric function varies with doping and model the Drude contribution to optical properties. We find that these Drude carrier densities and electrical conductivities are larger compared to the SLoT parameters, and we hypothesize that this could be because only the most electrically conductive and metal-like domains will have Drude like optical signatures, while the SLoT parameters weighted by the electrically insulating domains and are more indicative of macroscopic averages.

Moving forward, this study serves two primary purposes. First, we contextualized the SLoT transport parameters for PBTTT-$FeCl_3$ against other PBTTT studies and semiconducting polymer systems. This benchmark can be used moving forward to better quantify, understand, and compare other polymer-dopant-processing systems. Second, we showed how advanced scattering and spectroscopic measurements can be used in conjunction with SLoT to better understand transport properties. With additional SLoT, GIWAXS, and SE measurements, we can better quantify to what extent microstructure and inhomogeneity affect the resulting transport properties.

Supporting Information

Additional characterization procedures and measurements (PDF). SLoT measurements, calculations, and look-up table (XLSX).

Author Contributions

S.A.G. led optical and thermoelectric measurements, along with analysis of the results and preparing the manuscript. A.A. prepared thin films, collected and analyzed XPS data. J.F.P. prepared and characterized the PBTTT used in this study. G.F. collected and helped analyze GIWAXS data. G.M.S helped with GIWAXS data analysis and interpretation. M.D.L provided insight on and access to spectroscopic ellipsometry equipment and software. J.R.R. and S.K.Y. provided funding, access to equipment, and critical feedback. The authors would like to thank Joshua M. Rinehart for assistance with DSC measurements and procedures.

All authors participated in the preparation of this manuscript and agree on its final form.

ORCID

Shawn A. Gregory: 0000-0002-1027-0675

Amalie Atassi: 0000-0003-3218-680X

James F. Ponder Jr.: 0000-0001-8093-1849

John R. Reynolds: 0000-0002-7417-4869

Shannon K. Yee: 0000-0002-1119-9938

Guillaume Freychet: 0000-0001-8406-798X

Gregory M. Su: 0000-0001-7495-8041

Acknowledgments

S.A.G. appreciates the partial support from the Office of Naval Research (award no. N00014-19-1-2162), the Link Energy Foundation, and the Science and Technology of Material Interfaces (STAMI) group at the Georgia Institute of Technology. A.A. appreciates the support from the National Science Foundation (NSF) Graduate Research Fellowship. J.F.P., S.K.Y., and J.R.R are grateful for partial support from the Office of Naval Research (awards no. N00014-19-1-2162 and N00014-20-1-2129). Any opinions, findings and conclusions or recommendations expressed in this material are those of the authors and do not necessarily reflect the views of the NSF.

Part of this work (XPS analysis) was performed in part at the Georgia Tech Institute for Electronics and Nanotechnology, a member of the National Nanotechnology Coordinated Infrastructure, which is supported by the NSF (grant no. ECCS-1542174). Part of this work (GIWAXS) was performed at the beamline 12-ID of the National Synchrotron Light Source II, a U.S. Department of Energy (DOE) Office of Science User Facility operated for the DOE Office of Science by Brookhaven National Laboratory under Contract No. DE-SC0012704. The authors thanks Mikhail Zhernenkov (NSLS-II) for his assistance at the beamline.

Conflicts of Interest

There are no conflicts to declare.

References

1. Reynolds, J. R.; Thompson, B. C.; Skotheim, T. A., *Handbook of Conducting Polymers*. Marcel Dekker: 1998.
2. Kroon, R.; Mengistie, D. A.; Kiefer, D.; Hynynen, J.; Ryan, J. D.; Yu, L.; Muller, C., Thermoelectric plastics: from design to synthesis, processing and structure-property relationships. *Chem Soc Rev* **2016,** *45* (22), 6147-6164.
3. Bubnova, O.; Crispin, X., Towards polymer-based organic thermoelectric generators. *Energy & Environmental Science* **2012,** *5* (11), 9345–9362.
4. Russ, B.; Glaudell, A.; Urban, J. J.; Chabinyc, M. L.; Segalman, R. A., Organic thermoelectric materials for energy harvesting and temperature control. *Nature Reviews Materials* **2016,** *1* (10), 16050.
5. Sirringhaus, H., 25th Anniversary Article: Organic Field-Effect Transistors: The Path Beyond Amorphous Silicon. *Advanced Materials* **2014,** *26* (9), 1319-1335.
6. Bubnova, O.; Berggren, M.; Crispin, X., Tuning the Thermoelectric Properties of Conducting Polymers in an Electrochemical Transistor. *Journal of the American Chemical Society* **2012,** *134* (40), 16456-16459.
7. Kang, K.; Watanabe, S.; Broch, K.; Sepe, A.; Brown, A.; Nasrallah, I.; Nikolka, M.; Fei, Z.; Heeney, M.; Matsumoto, D.; Marumoto, K.; Tanaka, H.; Kuroda, S.; Sirringhaus, H., 2D coherent charge transport in highly ordered conducting polymers doped by solid state diffusion. *Nat Mater* **2016,** *15* (8), 896-902.
8. Chabinyc, M. L.; Toney, M. F.; Kline, R. J.; Mcculloch, I.; Heeney, M., X-ray Scattering Study of Thin Films of Poly(2,5-bis(3-alkylthiophen-2-yl)thieno[3,2-b]thiophene). *JACS* **2007,** *129*, 3226-3237.
9. Mcculloch, I.; Heeney, M.; Bailey, C.; Genevicius, K.; MacDonald, I.; Shkunov, M.; Sparrowe, D.; Tienry, S.; Wagner, R.; Zhang, W.; Chabinyc, M. L.; Kline, R. J.; McGehee, M. D.; Toney, M. F., Liquid-crystalline semiconducting polymers with high charge-carrier mobility. *Nature Materials* **2006,** *51*, 326-333.
10. Kang, K.; Schott, S.; Venkateshvaran, D.; Broch, K.; Schweicher, G.; Harkin, D.; Jellett, C.; Nielsen, C. B.; McCulloch, I.; Sirringhaus, H., Investigation of the thermoelectric response in conducting polymers doped by solid-state diffusion. *Materials Today Physics* **2019,** *8*, 112-122.
11. Vijayakumar, V.; Durand, P.; Zeng, H.; Untilova, V.; Herrmann, L.; Algayer, P.; Leclerc, N.; Brinkmann, M., Influence of dopant size and doping method on the structure and thermoelectric properties of PBTTT films doped with F6TCNNQ and F4TCNQ. *J. Mater. Chem. C* **2020,** *8*, 16470-16482.
12. Vijayakumar, V.; Zhong, Y.; Untilova, V.; Bahri, M.; Herrmann, L.; Biniek, L.; Leclerc, N.; Brinkmann, M., Bringing Conducting Polymers to High Order: Toward Conductivities beyond 105 S cm−1 and Thermoelectric Power Factors of 2 mW m−1 K−2. *Advanced Energy Materials* **2019,** *9* (24), 1900266.
13. Thomas, E. M.; Peterson, K. A.; Balzer, A. H.; Rawlings, D.; Stingelin, N.; Segalman, R. A.; Chabinyc, M. L., Effects of Counter-Ion Size on Delocalization of Carriers and Stability of Doped Semiconducting Polymers. *Adv. Electron. Mater.* **2020,** *6* (12), 2000595.
14. Thomas, E. M.; Popere, B. C.; Fang, H.; Chabinyc, M. L.; Segalman, R. A., Role of Disorder Induced by Doping on the Thermoelectric Properties of Semiconducting Polymers. *Chemistry of Materials* **2018,** *30* (9), 2965-2972.
15. Jacobs, I. E.; Lin, Y.; Huang, Y.; Ren, X.; Simatos, D.; Chen, C.; Tjhe, D.; Statz, M.; Lai, L.; Finn, P. A.; Neal, W. G.; D'Avino, G.; Lemaur, V.; Fratini, S.; Beljonne, D.; Strzalka, J.; Nielsen, C. B.; Barlow, S.; Marder, S. R.; McCulloch, I.; Sirringhaus, H., High-Efficiency Ion-Exchange Doping of Conducting Polymers. *Adv Mater* **2021**, e2102988.
16. Patel, S. N.; Glaudell, A. M.; Peterson, K. A.; Thomas, E. M.; O'Hara, K. A.; Lim, E.; Chabinyc, M. L., Morphology controls the thermoelectric power factor of a doped semiconducting polymer. *Science Advances* **2017,** *3* (6), e1700434.

17. Hisaaki Tanaka, K. K., Naoya Takekoshi, Hiroaki Mada, Hiroshi Ito, Yukihiro Shimoi, Hiromichi Ohta, Taishi Takenobu, Thermoelectric properties of a semicrystalline polymer doped beyond the insulator-to-metal transition by electrolyte gating. *Science Advances* **2020,** *6*, 1-8.
18. Durand, P.; Zeng, H.; Biskup, T.; Vijayakumar, V.; Untilova, V.; Kiefer, C.; Heinrich, B.; Herrmann, L.; Brinkmann, M.; Leclerc, N., Single Ether-Based Side Chains in Conjugated Polymers: Toward Power Factors of 2.9 mW m −1 K −2. *Advanced Energy Materials* **2021,** *2103049*, 1-11.
19. Huang, Y.; Lukito Tjhe, D. H.; Jacobs, I. E.; Jiao, X.; He, Q.; Statz, M.; Ren, X.; Huang, X.; McCulloch, I.; Heeney, M.; McNeill, C.; Sirringhaus, H., Design of experiment optimization of aligned polymer thermoelectrics doped by ion-exchange. *Applied Physics Letters* **2021,** *119* (11), 1-8.
20. Gregory, S. A.; Hanus, R.; Atassi, A.; Rinehart, J. M.; Wooding, J. P.; Menon, A. K.; Losego, M. D.; Snyder, G. J.; Yee, S. K., Quantifying charge carrier localization in chemically doped semiconducting polymers. *Nature Materials* **2021,** *20*, 1414–1421.
21. Gregory, S. A.; Ponder, J. F.; Pittelli, S. L.; Losego, M. D.; Reynolds, J. R.; Yee, S. K., Thermoelectric and Charge Transport Properties of Solution-Processable and Chemically Doped Dioxythienothiophene Copolymers. *ACS Applied Polymer Materials* **2021,** *3* (5), 2316–2324.
22. Zevalkink, A.; Smiadak, D. M.; Blackburn, J. L.; Ferguson, A. J.; Chabinyc, M. L.; Delaire, O.; Wang, J.; Kovnir, K.; Martin, J.; Schelhas, L. T.; Sparks, T. D.; Kang, S. D.; Dylla, M. T.; Snyder, G. J.; Ortiz, B. R.; Toberer, E. S., A practical field guide to thermoelectrics: Fundamentals, synthesis, and characterization. *Applied Physics Reviews* **2018,** *5* (2), 021303.
23. Kang, S. D.; Snyder, G. J., Charge-transport model for conducting polymers. *Nature Materials* **2017,** *16* (2), 252-257.
24. May, A. F.; Snyder, G. J., Introduction to modeling thermoelectric transport at high temperatures. In *Materials, Preparation, and Characterization in Thermoelectrics*, CRC Press: 2017.
25. Mott, N. F.; Davis, E. A., *Electronic processes in non-crystalline materials*. Oxford University Press: 2012.
26. Mott, N. F., The mobility edge since 1967. *J. Phys. C: Solid State Phys.* **1987,** *20*, 3075-3101.
27. Xuan, Y.; Liu, X.; Desbief, S.; Leclère, P.; Fahlman, M.; Lazzaroni, R.; Berggren, M.; Cornil, J.; Emin, D.; Crispin, X., Thermoelectric properties of conducting polymers: The case of poly(3-hexylthiophene). *Physical Review B* **2010,** *82* (11), 115454.
28. Noriega, R.; Rivnay, J.; Vandewal, K.; Koch, F. P.; Stingelin, N.; Smith, P.; Toney, M. F.; Salleo, A., A general relationship between disorder, aggregation and charge transport in conjugated polymers. *Nat Mater* **2013,** *12* (11), 1038-44.
29. Ponder, J. F., Jr.; Gregory, S. A.; Atassi, A.; Menon, A. K.; Lang, A. W.; Savagian, L. R.; Reynolds, J. R.; Yee, S. K., Significant Enhancement of the Electrical Conductivity of Conjugated Polymers by Post-Processing Side Chain Removal. *J Am Chem Soc* **2022,** *144* (3), 1351–1360.
30. Lim, E.; Glaudell, A. M.; Miller, R.; Chabinyc, M. L., The Role of Ordering on the Thermoelectric Properties of Blends of Regioregular and Regiorandom Poly(3-hexylthiophene). *Advanced Electronic Materials* **2019,** *5* (11), 1-11.
31. Fontana, M. T.; Stanfield, D. A.; Scholes, D. T.; Winchell, K. J.; Tolbert, S. H.; Schwartz, B. J., Evaporation vs Solution Sequential Doping of Conjugated Polymers: F4TCNQ Doping of Micrometer-Thick P3HT Films for Thermoelectrics. *The Journal of Physical Chemistry C* **2019,** *123* (37), 22711-22724.
32. Sezen-Edmonds, M.; Glaudell, A. M.; Chang, W. B.; Segalman, R. A.; Chabinyc, M. L.; Loo, Y.-L., Postdeposition Processing Influences the Relative Contributions of Electronic and Ionic Seebeck Effects in the Thermoelectric Response of Conducting Polymers. *The Journal of Physical Chemistry C* **2021,** *125* (22), 12289-12296.
33. Un, H.-I.; Gregory, S. A.; Mohapatra, S. K.; Xiong, M.; Longhi, E.; Lu, Y.; Rigin, S.; Jhulki, S.; Yang, C.-Y.; Timofeeva, T. V.; Wang, J.-Y.; Yee, S. K.; Barlow, S.; Marder, S. R.; Pei, J., Understanding the Effects

of Molecular Dopant on n-Type Organic Thermoelectric Properties. *Advanced Energy Materials* **2019,** *9* (24), 1900817.
34. Gregory, S. A.; Menon, A. K.; Ye, S.; Seferos, D. S.; Reynolds, J. R.; Yee, S. K., Effect of Heteroatom and Doping on the Thermoelectric Properties of Poly(3-alkylchalcogenophenes). *Advanced Energy Materials* **2018,** *8* (34), 1-8.
35. Gordon, M. P.; Gregory, S. A.; Wooding, J. P.; Ye, S.; Su, G. M.; Seferos, D. S.; Losego, M. D.; Urban, J. J.; Yee, S. K.; Menon, A. K., Microstructure and heteroatom dictate the doping mechanism and thermoelectric properties of poly(alkyl-chalcogenophenes). *Applied Physics Letters* **2021,** *118* (23), 1-8.
36. Al Kurdi, K.; Gregory, S. A.; Jhulki, S.; Conte, M.; Barlow, S.; Yee, S. K.; Marder, S. R., Electron transport in a sequentially doped naphthalene diimide polymer. *Materials Advances* **2020,** *1* (6), 1829-1834.
37. Vijayakumar, V.; Zaborova, E.; Biniek, L.; Zeng, H.; Herrmann, L.; Carvalho, A.; Boyron, O.; Leclerc, N.; Brinkmann, M., Effect of Alkyl Side Chain Length on Doping Kinetics, Thermopower, and Charge Transport Properties in Highly Oriented F4TCNQ-Doped PBTTT Films. *ACS Appl Mater Interfaces* **2019,** *11* (5), 4942-4953.
38. Zeier, W. G.; Zevalkink, A.; Gibbs, Z. M.; Hautier, G.; Kanatzidis, M. G.; Snyder, G. J., Thinking Like a Chemist: Intuition in Thermoelectric Materials. *Angew Chem Int Ed Engl* **2016,** *55* (24), 6826-41.
39. Kim, E. G.; Coropceanu, V.; Gruhn, N. E.; Sanchez-Carrera, R. S.; Snoeberger, R.; Matzger, A. J.; Bredas, J. L., Charge transport parameters of the pentathienoacene crystal. *J Am Chem Soc* **2007,** *129* (43), 13072-81.
40. Ma, T.; Dong, B. X.; Grocke, G. L.; Strzalka, J.; Patel, S. N., Leveraging Sequential Doping of Semiconducting Polymers to Enable Functionally Graded Materials for Organic Thermoelectrics. *Macromolecules* **2020,** *53* (8), 2882-2892.
41. Al Kurdi, K.; Gregory, S. A.; Gordon, M. P.; Ponder, J. F., Jr.; Atassi, A.; Rinehart, J. M.; Jones, A. L.; Urban, J. J.; Reynolds, J. R.; Barlow, S.; Marder, S. R.; Yee, S. K., Iron(III) Dopant Counterions Affect the Charge-Transport Properties of Poly(Thiophene) and Poly(Dialkoxythiophene) Derivatives. *ACS Appl Mater Interfaces* **2022,** *14* (25), 29039-29051.
42. Harris, J. K.; Neelamraju, B.; Ratcliff, E. L., Intersystem Subpopulation Charge Transfer and Conformational Relaxation Preceding in Situ Conductivity in Electrochemically Doped Poly(3-hexylthiophene) Electrodes. *Chemistry of Materials* **2019,** *31* (17), 6870-6879.
43. Shallcross, R. C.; Stubhan, T.; Ratcliff, E. L.; Kahn, A.; Brabec, C. J.; Armstrong, N. R., Quantifying the Extent of Contact Doping at the Interface between High Work Function Electrical Contacts and Poly(3-hexylthiophene) (P3HT). *The Journal of Physical Chemistry Letters* **2015,** *6* (8), 1303-1309.
44. Jacobs, I. E.; D'Avino, G.; Lemaur, V.; Lin, Y.; Huang, Y.; Chen, C.; Harrelson, T. F.; Wood, W.; Spalek, L. J.; Mustafa, T.; O'Keefe, C. A.; Ren, X.; Simatos, D.; Tjhe, D.; Statz, M.; Strzalka, J. W.; Lee, J. K.; McCulloch, I.; Fratini, S.; Beljonne, D.; Sirringhaus, H., Structural and Dynamic Disorder, Not Ionic Trapping, Controls Charge Transport in Highly Doped Conducting Polymers. *J Am Chem Soc* **2022,** *144* (7), 3005-3019.
45. Ashcroft, N.; Mermin, D., *Solid State Physics*. Cengage Learning: 1976.
46. Rivnay, J.; Mannsfeld, S. C.; Miller, C. E.; Salleo, A.; Toney, M. F., Quantitative determination of organic semiconductor microstructure from the molecular to device scale. *Chem Rev* **2012,** *112* (10), 5488-519.
47. Rivnay, J.; Noriega, R.; Kline, R. J.; Salleo, A.; Toney, M. F., Quantitative analysis of lattice disorder and crystallite size in organic semiconductor thin films. *Physical Review B* **2011,** *84* (4), 1-20.
48. Rivnay, J.; Noriega, R.; Northrup, J. E.; Kline, R. J.; Toney, M. F.; Salleo, A., Structural origin of gap states in semicrystalline polymers and the implications for charge transport. *Physical Review B* **2011,** *83* (12), 1-4.

49. Peng, Z.; Ye, L.; Ade, H., Understanding, quantifying, and controlling the molecular ordering of semiconducting polymers: from novices to experts and amorphous to perfect crystals. *Mater Horiz* **2021,** *9*, 577-606.
50. Abutaha, A.; Kumar, P.; Yildirim, E.; Shi, W.; Yang, S. W.; Wu, G.; Hippalgaonkar, K., Correlating charge and thermoelectric transport to paracrystallinity in conducting polymers. *Nat Commun* **2020,** *11* (1), 1737.
51. de Boor, J.; Muller, E., Data analysis for Seebeck coefficient measurements. *Rev Sci Instrum* **2013,** *84* (6), 065102.
52. Maddali, H.; House, K. L.; Emge, T. J.; O'Carroll, D. M., Identification of the local electrical properties of crystalline and amorphous domains in electrochemically doped conjugated polymer thin films. *RSC Advances* **2020,** *10* (36), 21454-21463.
53. Ma, T.; Dong, B. X.; Onorato, J. W.; Niklas, J.; Poluektov, O.; Luscombe, C. K.; Patel, S. N., Correlating conductivity and Seebeck coefficient to doping within crystalline and amorphous domains in poly(3-(methoxyethoxyethoxy)thiophene). *Journal of Polymer Science* **2021,** *59* (22), 2797-2808.
54. Boyle, C. J.; Upadhyaya, M.; Wang, P.; Renna, L. A.; Lu-Diaz, M.; Pyo Jeong, S.; Hight-Huf, N.; Korugic-Karasz, L.; Barnes, M. D.; Aksamija, Z.; Venkataraman, D., Tuning charge transport dynamics via clustering of doping in organic semiconductor thin films. *Nat Commun* **2019,** *10* (1), 2827.
55. Yu, Y.; Zhou, C.; Zhang, S.; Zhu, M.; Wuttig, M.; Scheu, C.; Raabe, D.; Snyder, G. J.; Gault, B.; Cojocaru-Mirédin, O., Revealing nano-chemistry at lattice defects in thermoelectric materials using atom probe tomography. *Materials Today* **2020,** *32*, 260-274.
56. Ponder Jr, J. F.; Chen, H.; Luci, A. M. T.; Moro, S.; Turano, M.; Hobson, A. L.; Collier, G. S.; Perdigão, L. M. A.; Moser, M.; Zhang, W.; Costantini, G.; Reynolds, J. R.; McCulloch, I., Low-Defect, High Molecular Weight Indacenodithiophene (IDT) Polymers Via a C–H Activation: Evaluation of a Simpler and Greener Approach to Organic Electronic Materials. *ACS Materials Letters* **2021,** *3* (10), 1503-1512.
57. Slade, T. J.; Grovogui, J. A.; Kuo, J. J.; Anand, S.; Bailey, T. P.; Wood, M.; Uher, C.; Snyder, G. J.; Dravid, V. P.; Kanatzidis, M. G., Understanding the thermally activated charge transport in NaPbmSbQm+2 (Q = S, Se, Te) thermoelectrics: weak dielectric screening leads to grain boundary dominated charge carrier scattering. *Energy & Environmental Science* **2020,** *13* (5), 1509-1518.
58. Kuo, J. J.; Kang, S. D.; Imasato, K.; Tamaki, H.; Ohno, S.; Kanno, T.; Snyder, G. J., Grain boundary dominated charge transport in Mg3Sb2-based compounds. *Energy & Environmental Science* **2018,** *11* (2), 429-434.
59. Peterseim, T.; Dressel, M.; Dietrich, M.; Polity, A., Optical properties of VO2 films at the phase transition: Influence of substrate and electronic correlations. *Journal of Applied Physics* **2016,** *120* (7), 1-6.
60. Gaiser, P.; Binz, J.; Gompf, B.; Berrier, A.; Dressel, M., Tuning the dielectric properties of metallic-nanoparticle/elastomer composites by strain. *Nanoscale* **2015,** *7* (10), 4566-71.
61. Hövel, M.; Gompf, B.; Dressel, M., Dielectric properties of ultrathin metal films around the percolation threshold. *Physical Review B* **2010,** *81* (3), 1-8.
62. Leick, N.; Weber, J. W.; Mackus, A. J. M.; Weber, M. J.; van de Sanden, M. C. M.; Kessels, W. M. M., In situspectroscopic ellipsometry during atomic layer deposition of Pt, Ru and Pd. *Journal of Physics D: Applied Physics* **2016,** *49* (11), 1-12.
63. Hanus, R.; Gregory, S. A.; Adams, M. J.; Graham, S.; Yee, S. K., Quantifying the Effects of Inhomogeneity and Doping on the Electronic Contribution to Thermal Conductivity in Semiconducting Polymers. *Advanced Electronic Materials* **2022,** *8*, 1-8.
64. Mildred Dresselhaus; Gene Dresselhaus; Stephen Cronin; Antonio Gomes; Filho, S., *Solid State Properties: From Bulk to Nano*. Springer: 2018.
65. Kasap, S. O., *Principles of Electronic Materials and Devices*. McGraw-Hill Education: 2005.

66. Cobet, C.; Oppelt, K.; Hingerl, K.; Neugebauer, H.; Knör, G.; Sariciftci, N. S.; Gasiorowski, J., Ellipsometric Spectroelectrochemistry: An in Situ Insight in the Doping of Conjugated Polymers. *The Journal of Physical Chemistry C* **2018,** *122* (42), 24309-24320.
67. Gasiorowski, J.; Hingerl, K.; Menon, R.; Plach, T.; Neugebauer, H.; Wiesauer, K.; Yumusak, C.; Sariciftci, N. S., Dielectric Function of Undoped and Doped Poly[2-methoxy-5-(3',7'-dimethyloctyloxy)-1,4-phenylene-vinylene] by Ellipsometry in a Wide Spectral Range. *J Phys Chem C Nanomater Interfaces* **2013,** *117* (42), 22010-22016.
68. Vezie, M. S.; Few, S.; Meager, I.; Pieridou, G.; Dorling, B.; Ashraf, R. S.; Goni, A. R.; Bronstein, H.; McCulloch, I.; Hayes, S. C.; Campoy-Quiles, M.; Nelson, J., Exploring the origin of high optical absorption in conjugated polymers. *Nat Mater* **2016,** *15* (7), 746-53.
69. Bednarski, H.; Hajduk, B.; Jurusik, J.; Jarząbek, B.; Domański, M.; Łaba, K.; Wanic, A.; Łapkowski, M., The Influence of PEDOT to PSS Ratio on the Optical Properties of PEDOT:PSS Thin Solid Films - Insight from Spectroscopic Ellipsometry. *Acta Physica Polonica A* **2016,** *130* (5), 1242-1244.
70. Schubert, M.; Bundesmann, C.; Jakopic, G.; Maresch, H.; Arwin, H.; Persson, N. C.; Zhang, F.; Inganäs, O., Infrared ellipsometry characterization of conducting thin organic films. *Thin Solid Films* **2004,** *455-456*, 295-300.
71. Chen, S.; Kang, E. S. H.; Shiran Chaharsoughi, M.; Stanishev, V.; Kuhne, P.; Sun, H.; Wang, C.; Fahlman, M.; Fabiano, S.; Darakchieva, V.; Jonsson, M. P., Conductive polymer nanoantennas for dynamic organic plasmonics. *Nat Nanotechnol* **2020,** *15* (1), 35-40.
72. Girtan, M.; Mallet, R.; Socol, M.; Stanculescu, A., On the Physical Properties PEDOT:PSS Thin Films. *Materials Today Communications* **2020,** *22*, 1-8.
73. Chen, S.; Kühne, P.; Stanishev, V.; Knight, S.; Brooke, R.; Petsagkourakis, I.; Crispin, X.; Schubert, M.; Darakchieva, V.; Jonsson, M. P., On the anomalous optical conductivity dispersion of electrically conducting polymers: ultra-wide spectral range ellipsometry combined with a Drude–Lorentz model. *Journal of Materials Chemistry C* **2019,** *7* (15), 4350-4362.
74. Woollam, J. A. Ellipsometry Resources. https://www.jawoollam.com/resources (accessed 2023-02-01).
75. Price, J.; Hung, P. Y.; Rhoad, T.; Foran, B.; Diebold, A. C., Spectroscopic ellipsometry characterization of HfxSiyOz films using the Cody–Lorentz parameterized model. *Applied Physics Letters* **2004,** *85* (10), 1701-1703.
76. Moulé, A. J.; Gonel, G.; Murrey, T. L.; Ghosh, R.; Saska, J.; Shevchenko, N. E.; Denti, I.; Fergerson, A. S.; Talbot, R. M.; Yacoub, N. L.; Mascal, M.; Salleo, A.; Spano, F. C., Quantifying Polaron Mole Fractions and Interpreting Spectral Changes in Molecularly Doped Conjugated Polymers. *Advanced Electronic Materials* **2021,** *2100888*, 1-9.
77. Ponder, J. F., Jr.; Gregory, S. A.; Atassi, A.; Advincula, A. A.; Rinehart, J. M.; Freychet, G.; Su, G. M.; Yee, S. K.; Reynolds, J. R., Metal-like Charge Transport in PEDOT(OH) Films by Post-processing Side Chain Removal from a Soluble Precursor Polymer. *Angew Chem Int Ed Engl* **2023,** *62* (1), e202211600.